Journal of Geophysical Research: Solid Earth

RESEARCH ARTICLE
10.1029/2018JB016113

Special Section:
Merging Geophysical, Petrochronologic and Modeling Perspectives to Understand Large Silicic Magma Systems

# Slug Stability in Flaring Geometries and Ramifications for Lava Lake Degassing

**Zhipeng Qin[1], Arianna Soldati[2,3], Liannie C. Velazquez Santana[4,5], Alison C. Rust[6], Jenny Suckale[1], and Katharine V. Cashman[6]**

[1]Department of Geophysics, Stanford University, Stanford, CA, USA, [2]Department of Geological Sciences, University of Missouri, Columbia, MO, USA, [3]Now at Department of Earth and Environmental Sciences, Ludwig-Maximilians-Universitat Munchen, Munich, Germany, [4]Department of Geology, University of Puerto Rico, Mayaguez, Puerto Rico, [5]Department of Geology and Environmental Earth Science, Miami University, Oxford, OH, USA, [6]School of Earth Sciences, University of Bristol, Bristol, UK

**Key Points:**
- The rapid change in the geometry associated with the transition from the conduit to the lava lake causes large gas slugs to break up
- Stability of the gas slug depends sensitively on the geometry and on the Reynolds number
- Most lava lakes fall well within the regime where large gas slugs are prone to breakup

**Supporting Information:**
- Supporting Information S1

**Correspondence to:**
Z. Qin,
zhipengq@stanford.edu

**Citation:**
Qin, Z., Soldati, A., Santana, L. C. V., Rust, A., Suckale, J., & Cashman, K. V. (2018). Slug stability in flaring geometries and ramifications for lava lake degassing. *Journal of Geophysical Research: Solid Earth*, *123*. https://doi.org/10.1029/2018JB016113

Received 16 MAY 2018
Accepted 18 NOV 2018
Accepted article online 22 NOV 2018



**Abstract** Long-lived, persistently active lava lakes are rare but have been studied extensively because they may provide a natural laboratory for studying magmatic convection in basaltic and other low-viscosity volcanoes. However, lava lakes differ from other volcanic systems in various ways, particularly geometry: the presence of the lava lake requires a sudden and significant flaring of the conduit. The goal of this paper is to advance our understanding of the effect that a sudden increase in the conduit width has on the stability of large gas slugs and bubbles ascending from the plumbing system. We investigate this question by linking analog laboratory experiments to direct numerical simulations in two dimensions. We find that the rapid change in the geometry associated with the transition from the conduit to the lava lake causes large gas slugs to break up. The nondimensional regime over which we observe the breakup depends sensitively on the flare angle of the lava lake and the importance of inertial effects in the flow, implying that degassing-related eruptive activity at open-system volcanoes is sensitive to the upper conduit and lake geometries. Applying this idea to the likely geometries and viscosities of actual lava lakes, our study suggests that all lava lakes except Erebus fall well within the regime where large gas slugs are prone to breakup.

## 1. Introduction

Active lava lakes occur on volcanoes with basaltic or other relatively low-viscosity melt compositions like phonolite. The low melt viscosity allows gas bubbles to segregate from the magma flow easily and rise to the surface. The associated high gas flux drives constant recirculation of the degassing magma, through which the system maintains high heat flux and degasses continually (e.g., Wilson & Head, 1981). Despite the persistent degassing, lava lakes exhibit a wide range of eruptive behavior, from passive and persistent gas loss to energetic explosions, fountaining, and strong gas jetting (Allard et al., 2016; Daly, 1911; Dibble et al., 2008; Johnson et al., 2008; Oppenheimer et al., 2009; Patrick et al., 2011; Perret, 1913).

Recognizing the importance of a separate gas phase, many existing models for lava lakes, and basaltic volcanism more generally, link eruptive behavior to the two-phase interactions between gas and silicate melt as reviewed in Vergniolle and Mangan (2000). Mechanisms that could contribute to the episodic eruptions observed at many lava lakes include gas pistoning (e.g., Patrick et al., 2011; Swanson et al., 1979), dynamic pressure equilibration (e.g., Witham et al., 2006), unstable bidirectional conduit flow (e.g., Oppenheimer et al., 2009), and the intermittent rise of large gas slugs (e.g., Blackburn et al., 1976; Jaupart & Vergniolle, 1989; Wilson & Head, 1981). Of these mechanisms, the slug model has been most commonly invoked (e.g., Allard et al., 2016; Aster et al., 2003; Bouche et al., 2010; Calder et al., 2004; Gerst et al., 2013; Johnson et al., 2008; Pyle et al., 1995; Vergniolle & Jaupart, 1990).

The present study builds on the idea that episodic Strombolian-type eruptions at lava lakes may represent the intermittent rise and burst of large gas slugs at the free surface of the lava (e.g., Vergniolle & Jaupart, 1990). The slugs, or Taylor bubbles, are thought to form either in the magma chamber through foam collapse (Jaupart & Vergniolle, 1989) or in the conduit via coalescence of bubbles driven by differential ascent speed (Parfitt & Wilson, 1995), and to then rise through the conduit and exit through the lava lake. In the original

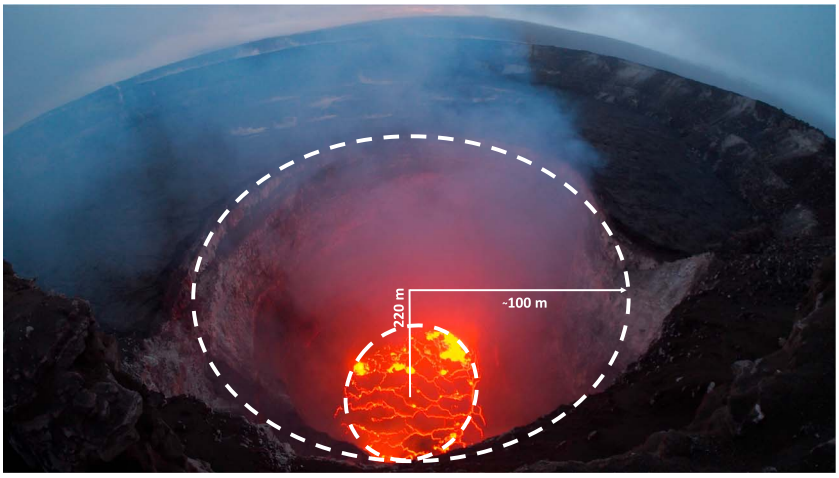


**Figure 1.** Camera view of Halemaumau lava lake on 6 May 2018 (by U.S. Geological Survey) and the estimation of the geometry. The recent draining of magma exposed the geometry of the former (now drained) lava lake. The lava lake had dropped to 220 m below the crater rim when this picture was taken. We estimate that the flare angle of the lava lake is larger than 30°.

experiment reproducing slug formation (Jaupart & Vergniolle, 1989), the conduit is represented as a vertical perfect pipe. The conduits of volcanoes hosting active lava lakes, however, widen significantly toward the surface. For example, the recent eruption on Hawaii drained the Halemaumau lava lake rapidly and revealed its geometry in a spectacular way (e.g., Figure 1).

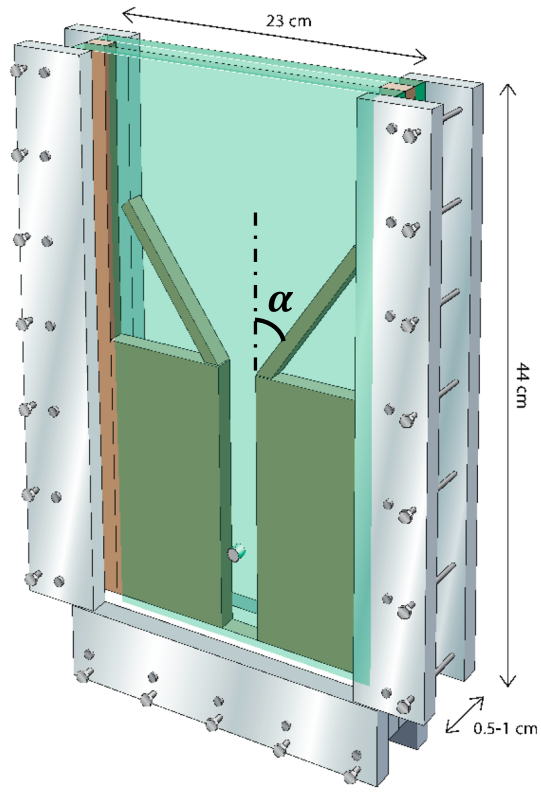


**Figure 2.** Technical drawing of the experimental apparatus. The outer structure is a transparent Hele-Shaw cell (44 × 23 × 1 cm); polyvinyl chloride parallelepipeds and sticks of different lengths and angled ends outline different system configurations. Bubbles are injected with a syringe through a hole in the front plate. Courtesy of Simon Powell.

To better understand how the flaring geometry of a lava lake affects slug behavior, we designed an experimental apparatus that reproduces the transition between a narrow conduit at depth and a lava lake that flares out toward the free surface (see Figure 2). In the interest of simplicity, we adopt a two-dimensional geometry. A two-dimensional point of view is most appropriate for an axisymmetric lava lake and a circular conduit but may also provide a reasonable starting point for understanding the stability of slugs passing through flares in more general geometries. Instead of being generated dynamically, the gas slugs in our experiments are injected directly into the conduit. With this apparatus, we can vary the slope of the side walls to analyze the effect of the flare angle, $\alpha$, on slug stability.

Throughout the manuscript, we define the angle of the flare as the angle between the vertical direction and the sloping side wall (see Figure 2). With this definition, a high-angle flare corresponds to significant widening with $\alpha = 90°$ indicating a discontinuous change in diameter, and a small-angle flare represents a small degree of widening approaching a conduit with a constant diameter at $\alpha = 0°$. The variability of the flare angle enables us to investigate the full range of possible flare angles to understand the importance of this parameter for slug stability. Thus, the experimental apparatus is not meant to represent a specific lava lake exactly to scale but is designed to capture a wide range of nondimensional regimes.

We upscale our analog experiments to a wider nondimensional regime than achievable in the laboratory with direct numerical simulations following the methodology of Qin and Suckale (2017). The simulations are direct in the sense that they do not require any fitting parameters. Instead, the flow dynamics emerges self-consistently based on the fluid properties and apparatus geometry alone. Our numerical approach solves the Navier-Stokes equation in both phases, while accounting for the dramatic material differences between the gas and liquid that produce

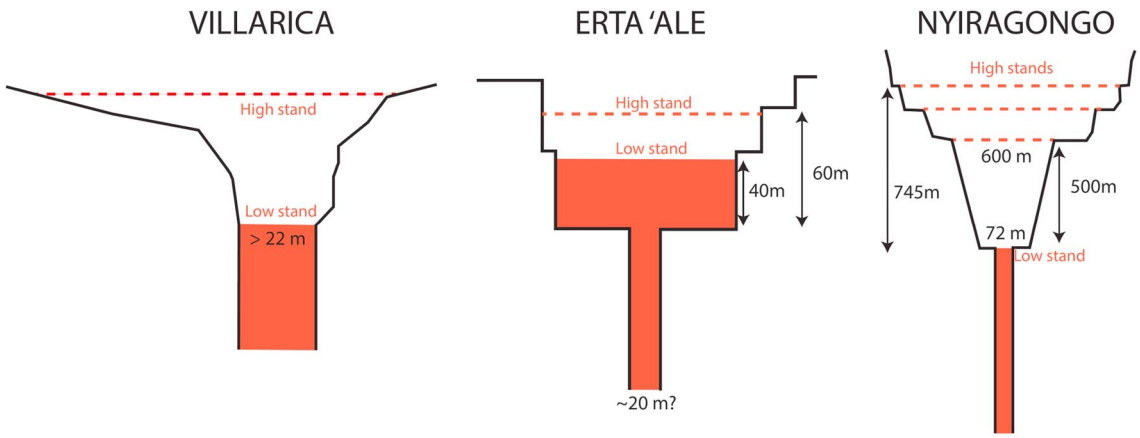


**Figure 3.** Schematics of lava lakes at Villarica (from Moussallam et al., 2013), Era 'Ale (from Bouche et al., 2010, the conduit diameter is uncertain), and Nyrangongo (from Burgi et al., 2014).

discontinuities in the pressure and stress (e.g., Qin & Suckale, 2017; Suckale, Nave, & Hager, 2010). The interface between gas and liquid can evolve freely, which implies that gas bubbles can break up or coalesce dynamically. The numerical methodology has been verified and validated extensively in prior studies (e.g., Qin & Suckale, 2017; Suckale, Nave, & Hager, 2010).

Previous studies have demonstrated that conduit geometry may play an important role in modulating the rise of large gas slugs (e.g., Ambrose et al., 2017; James et al., 2006; Pioli et al., 2009). James et al. (2006) performed experiments of slug ascent through vertical tubes with a smooth change in the diameter. For the set of conditions tested, the authors found that when the upper tube was narrower, the rising bubble deformed but did not break up when passing through the constriction. Breakup did tend to occur, however, when the slugs rose from a narrow to a wider tube (James et al., 2006).

Building on this work, we investigate how the presence of a lava lake at the upper portion of the conduit may alter the stability of large gas slugs. We hypothesize that the tendency of large gas slugs to break up depends sensitively on the angle of the flare. We define breakup as the process of at least one daughter bubble splitting off from the initial slug. In many cases, the volume of the daughter bubbles is much smaller than that of the main slug. Importantly, the occurrence of breakup does not necessarily imply that large slugs do not exist, but it may significantly limit the aspect ratio that slugs may attain. Given the simplified setup of our experiments, our study constrains only the onset of instability, which is likely exacerbated by factors not considered in this study but potentially important in nature, such as lava lake convection and the presence of crystals or faltering lava lake skin.

An important motivation for this work is the observation that the geometry of many lava lakes varies with depth. Examples include (1) Villarica, Chile (Moussallam et al., 2016), (2) Erta Ale, Ethiopia (Bouche et al., 2010), and (3) Nyiragongo, Democratic Republic of Congo (Burgi et al., 2014). Other lava lakes may exhibit this behavior as well, but their geometry is less well constrained. Schematic cross sections of all three lava lakes are shown in Figure 3. We hypothesize that the abrupt change in the geometry that accompanies different degrees of filling in the lava lake could trigger a similarly abrupt change in the degassing patterns if the system transitions from a geometry in which slugs are stable to one in which slugs experience breakup upon rise or lowering of the magma level. Changes in bubble stability could affect the associated acoustic and seismic signals, including very low period signals (e.g., James et al., 2006).

The geometry of the upper parts of the lakes are at least partially constrained by direct observations. All three retain evidence of high stands in the form of platforms that circle the inner crater. Only for Villarica, however, has the lower portion of the lava lake been observed directly as well. In this case, the connection between the conduit exhibits a low-angle flare that indicates a very gradual transition from the lake to the conduit. A similar low-angle flare can be seen in photographs of the phonolitic lava lake on Mount Erebus (Dibble et al., 2008) and during the recent eruption at Halemaumau lava lake, Hawaii (see Figure 1). In contrast, Erta Ale and Nyiragongo lava lakes are characterized by a rapid widening of the conduit that indicates very high angle flares (see Figure 3).

**Table 1**
*Experiment Conditions*

| $\alpha$ (deg) | $V$ (ml) | AR | $\mu$ (Pa s) | $N_f$ | Upside exp string | Upside-down exp string | Figure # |
|---|---|---|---|---|---|---|---|
| 75 | 1 | 0.7 | 49 | 0.5 | 75-1-p | | 5 |
| | 5 | 3.5 | | | 75-5-p | | 5 |
| | 8 | 5.6 | | | 75-8-p | | 5 |
| | 9 | 6.3 | | | 75-9-p | | 5,13,16 |
| | 10 | 7.0 | | | 75-10-p | | 5,15,16 |
| | 15 | 10.0 | | | 75-15-p | | 3,5,11,13,16 |
| 60 | 1 | 0.7 | 49 | 0.5 | 60-1-p | | 5 |
| | 5 | 3.5 | | | 60-5-p | | 5 |
| | 8 | 5.6 | | | 60-8-p | | 5 |
| | 9 | 6.3 | | | 60-9-p | | 5 |
| | 10 | 7.0 | | | 60-10-p | | 5,13,15,16 |
| | 15 | 10.5 | | | 60-15-p | | 5,13,16 |
| 45 | 1 | 0.7 | 49 | 0.5 | 45-1-p | | 5 |
| | 5 | 3.5 | | | 45-5-p | | 5 |
| | 8 | 5.6 | | | 45-8-p | | 5 |
| | 9 | 6.3 | | | 45-9-p | | 5 |
| | 10 | 7.0 | | | 45-10-p | | 5,13,15,16 |
| | 15 | 10.5 | | | 45-15-p | | 5, 13, 16 |
| 30 | 1 | 0.7 | 49 | 0.5 | 30-1-p | | 5 |
| | 5 | 3.5 | | | 30-5-p | | 5 |
| | 8 | 5.6 | | | 30-8-p | | 5 |
| | 9 | 6.3 | | | 30-9-p | | 4,5,13,16 |
| | 10 | 7.0 | | | 30-10-p | | 5,15 |
| | 15 | 10.5 | | | 30-15-p | | 5,13,16 |
| 75 | 1 | 0.7 | 17 | 1 | 75-1-d | UD-75-1-d | 10 |
| | 5 | 3.5 | | | 75-5-d | UD-75-5-d | 10 |
| | 8 | 5.6 | | | 75-8-d | | 5 |
| | 9 | 6.3 | | | 75-9-d | | 5,13,16 |
| | 10 | 7.0 | | | 75-10-d | UD-75-10-d | 9, 10 |
| | 15 | 10.5 | | | 75-15-d | UD-75-15-d | 10 |

We link these geometrical constraints to measurements of lava viscosity and magma density at different lava lakes. From these material properties, we can estimate the relative importance of viscous to inertial effects as captured in the Reynolds number, or equivalently, in the inverse viscosity number. We then explore how slug stability over the range of nondimensional numbers determined for the different lava lakes. Although there is significant uncertainty in the lava viscosity, the majority of lava lakes fall well into the nondimensional regime where inertial effects become important and slug breakup common. The exception is Ray Lake at Mount Erebus, Antarctica, where the flow dynamics is likely dominated by viscosity.

## 2. Methodology

### 2.1. Experimental Materials and Method

The experimental apparatus (Figure 2) is a Hele-Shaw cell, that is, a thin parallelepiped device commonly used to model fluid behavior in 2-D. The apparatus consists of two vertical 27-cm-wide by 46-cm-high transparent acrylic plates that are clamped together with a right-angled U-shaped polyvinyl chloride (PVC) spacer along the base and two sides (but not the top) of the plates. Most experiments were run with a 1-cm-thick spacer, forming a 23-cm × 44-cm × 1-cm gap between the plates; data were also collected with a 0.5-cm-thick spacer (see supporting information). Various system configurations were constructed, each with a pair of PVC

**Table 1**
*Continued*

| $\alpha$ (deg) | $V$ ml | AR | $\mu$ Pa s | $N_f$ | Upside exp string | Upside-down exp string | Figure # |
|---|---|---|---|---|---|---|---|
| 60 | 1 | 0.7 | 17 | 1 | 60-1-d | UD-60-1-d | 10 |
| | 5 | 3.5 | | | 60-5-d | UD-60-5-d | 10 |
| | 8 | 5.6 | | | 60-8-d | | 5 |
| | 9 | 6.3 | | | 60-9-d | | 5,13,15,16 |
| | 10 | 7.0 | | | 60-10-d | UD-60-10-d | 10 |
| | 15 | 10.5 | | | 60-15-d | UD-60-15-d | 10 |
| 45 | 1 | 0.7 | 17 | 1 | 45-1-d | UD-45-1-d | 10 |
| | 5 | 3.5 | | | 45-5-d | UD-45-5-d | 10 |
| | 8 | 5.6 | | | 45-8-d | | 5 |
| | 9 | 6.3 | | | 45-9-d | | 5,13,15,16 |
| | 10 | 7.0 | | | 45-10-d | UD-45-10-d | 10 |
| | 15 | 10.5 | | | 45-15-d | UD-45-15-d | 10 |
| 30 | 1 | 0.7 | 17 | 1 | 30-1-d | UD-30-1-d | 10 |
| | 5 | 3.5 | | | 30-5-d | UD-30-5-d | 10 |
| | 8 | 5.6 | | | 30-8-d | | 4,5,13,16 |
| | 9 | 6.3 | | | 30-9-d | | 5,15 |
| | 10 | 7.0 | | | 30-10-d | UD-30-10-d | 8,10 |
| | 15 | 10.5 | | | 30-15-d | UD-30-15-d | 10 |

*Note.* Apparatus thickness is 1 cm. Flare angle ($\alpha$), gas volume ($V$), and corresponding aspect ratio, (AR), viscosity of liquid ($\mu$), and the dimensionless inverse viscosity, upside experiment string, upside-down experiment string, and the number of figures where the corresponding experiments and/or their numerical reproductions are shown.

parallelepipeds and a pair of rectangular sticks with angled ends. All PVC components were the same thickness as the spacer and were clamped with the spacer between the acrylic plates. Specifically, the experimental apparatus was set to have a 20-cm-long, 3-cm-wide, and 1-cm-thick channel (between the PVC parallelepipeds) terminating in a symmetrically flared region with sticks oriented at a slope to create flare angles of (a) 75°, (b) 60°, (c) 45°, or (d) 30°. We also performed *upside-down* experiments with a constriction formed by sticks at angles of (a) 75°, (b) 60°, (c) 45°, or (d) 30°, topped by a 20-cm-long, 3-cm-wide, and 1-cm-thick channel. Once assembled, the gap was filled with syrup. Experimental conditions are summarized in Table 1.

We used Tate and Lyle pure ($\mu = 49$ Pa s) or water-diluted ($\mu = 17$ Pa s) golden syrup as analog silicate melt. Golden syrup is a Newtonian liquid with well-known properties that is often used to model magma (e.g., Bagdassarov & Pinkerton, 2004). The syrup viscosity was measured with a Thermo Scientific HAAKE MARS II Rotational Rheometer with rotating cylinder geometry. All viscosity measurements and experiments were performed at a controlled temperature of 18 °C ± 1 °C. The densities of the golden syrup and the water-diluted golden syrup were 1,430 kg/m$^3$ and 1,425 kg/m$^3$, respectively (Table 1 in Beckett et al., 2011). The surface tension between air and syrup is around 0.08 N/m (Borhan & Pallinti, 1999; Llewellin et al., 2002; Rust & Manga, 2002). We assume that this value was suitable for the golden syrup and the water-diluted golden syrup.

The experimental apparatus was filled from the top with the golden syrup. To remove air bubbles introduced into the syrup during the filling process, the apparatus was left to degas for at least 12 hr with a plastic film covering the top to prevent syrup dehydration. We used air as analog volcanic gas. The front transparent acrylic plate had a hole in the middle 5 cm from the bottom. A syringe equipped with a hypodermic needle (diameter = 0.8 mm) connected to the hole allowed manual injection of conduit-filling gas slugs (the ratio between the bubble and the channel diameter greater than 0.6) into the apparatus. We varied the slug volume between 1 and 18 ml.

All experiments were filmed with a Sony Handycam HDR-SR5 video camera mounted on a tripod directly facing the experimental apparatus. The free video analysis and modeling tool Tracker 4.75.00 was used to determine the time-space coordinates of the rising bubbles. The origin of the Cartesian reference system was

set in the center of the channel at the slope break level; the intersection between the vertical and the slope defined the flare angle, $\alpha$. Time $t_0$ was defined as the time when the bubble head reached the slope break, that is, when $y = 0$. The time interval between consecutive frames is 1/5 s. The vertical speed was calculated as the first derivative of $y$ with respect to time. Data were filtered through a running average over 13 data points, so as to adequately trace the bubble motion without the influence of the oscillations caused by imprecise synchronization of the video camera's internal clock. The public domain Java image processing program ImageJ 1.4.3.67 was used to calculate the bubble size (area) and to monitor size changes during each experiment. Some of the experiment results were published without our knowledge or consent by Ambrose et al. (2017).

### 2.2. Numerical Model

Our 2-D numerical model solves the governing equations for conserving mass and momentum in the gas and the liquid. We assume that the gas and the liquid are incompressible. Although there is little doubt that compressibility is important for volcanic processes in general, in this study we are particularly interested in understanding slug stability upon passage from a conduit to a lava lake. As demonstrated in more detail in the supporting information, the pressure variations on the slug interface at this instance are very small, at the laboratory and volcano scales. Therefore, we argue that it is reasonable to expect that compressibility would not alter slug stability in a significant way.

With these assumptions, the governing equations reduce to incompressibility,

$$\nabla \cdot \mathbf{v} = 0\,, \tag{1}$$

and the variable-coefficient Navier-Stokes equation

$$\rho\left(\frac{\partial \mathbf{v}}{\partial t} + (\mathbf{v}\cdot\nabla)\mathbf{v}\right) = -\nabla p + \nabla\cdot\left[\mu(\nabla\mathbf{v} + (\nabla\mathbf{v})^T)\right] + \rho\mathbf{g}\,,$$

where $\mathbf{v}$ is the velocity, $p$ the pressure, $\mathbf{g}$ the gravitational acceleration, $\rho$ the density, and $\mu$ the dynamic viscosity. The code tracks the dynamic evolution of the gas-liquid interface without limiting its deformability or restricting topological change as might occur during rupture or coalescence (Qin & Suckale, 2017; Suckale, Nave, Hager, et al., 2010) through a level set approach (Osher & Sethian, 1988). This leads to an advection equation for the gas-liquid interface

$$\frac{\partial \phi}{\partial t} + \mathbf{v}\cdot\nabla\phi = 0\,, \tag{2}$$

where $\phi$ indicates a level set function whose zero level represents the gas-liquid interface. We assume that both the pure liquid and the gas phase are Newtonian fluids. Non-Newtonian properties of the bubbly mixture arise exclusively from phase interactions.

The material properties change discontinuously at the interface between the gas and the liquid. For example, we define the density as

$$\rho(\mathbf{x}) = \begin{cases} \rho_l & \phi > 0 \\ \rho_g & \phi \le 0 \end{cases}\,, \tag{3}$$

where the subscripts $l$ and $g$ refer to the liquid and the gas, respectively. The viscosity is defined analogously.

The jump conditions at the gas-liquid interface reflect the combined effect of the surface tension and stresses,

$$\left[\begin{pmatrix} \mathbf{n} \\ \mathbf{t}_1 \\ \mathbf{t}_2 \end{pmatrix}(pI - \tau)\mathbf{n}^{\mathrm{T}}\right] = \begin{pmatrix} \sigma\kappa \\ 0 \\ 0 \end{pmatrix}\,, \tag{4}$$

where $I$ is the identity matrix, $\tau = \mu\left(\nabla\mathbf{v} + (\nabla\mathbf{v})^T\right)$ is the stress tensor, $\sigma$ the surface tension, $\kappa$ the curvature of $\Gamma$, $\mathbf{n}$ the unit normal vector on $\Gamma$ that is directed from gas toward liquid, and $\mathbf{t}_1$ and $\mathbf{t}_2$ are the two unit tangential vectors.

Figure 4 illustrates the grid setup for our numerical model, where the 2-D geometry mimics the experimental apparatus shown in Figure 2. We solve the governing equation in the fluid portion (white) of the domain and apply a no-slip boundary condition on the solid walls (black). To discretize the governing equation on a Cartesian grid, we apply the numerical method recently developed and validated by Qin and Suckale (2017), which was designed specifically to capture the complex multiphase behavior in volcanic systems where dramatic variations in viscosity and density are common.

The numerical approach consists of three main components. The first component is a time-step splitting Navier-Stokes solver that can handle density and viscosity differences of orders of magnitude occurring

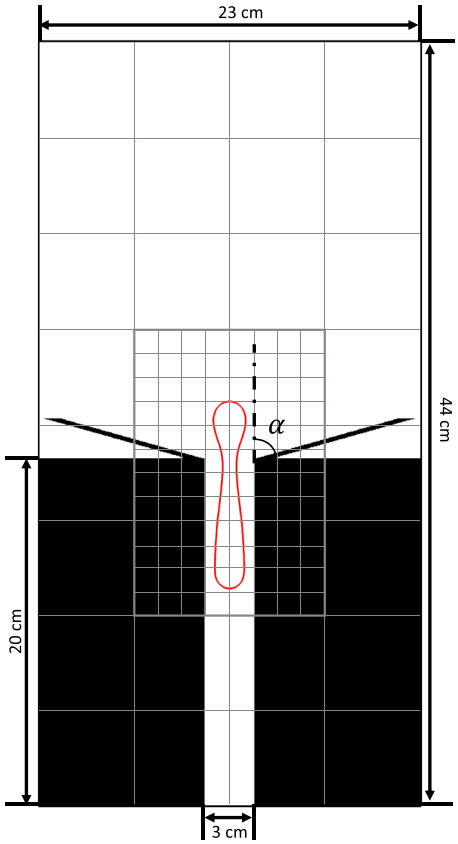


**Figure 4.** Setup of the two grids. Around the gas slug (red), we refine the grid to capture the interaction between the bubble and flared solid structure (black). The refinement ratio here is 4.

discontinuously at the gas-liquid interface through an implicit implementation of the viscous term. The computational efficiency of this solver is maintained with approximate factorization of the resulting sparse matrices. The second component is a level-set-based interface solver that tracks the motion of the liquid-liquid interface through an iterative topology-preserving projection (Qin et al., 2015). A particular advantage of the interface solver lies in its ability to accurately compute surface tension on dynamically evolving interfaces. The third component is an adaptive mesh refinement that evolves with the moving gas bubble (see Figure 4). The locally refined grid allows us to capture instability of the gas-liquid interface more accurately and efficiently than possible on a standard Cartesian grid.

Although the flow in the Hele-Shaw cell is 2-D, the acrylic plates exert a shear stress in the third dimension. For a quantitative comparison between the laboratory and the computations, this shear stress needs to be incorporated into the computations. Thus, we add a wall stress term, $\tau_w$, to the momentum equation (see equation (2.2)). In the laminar regime, where the speed profile is parabolic, we approximate the wall stress term as

$$\tau_w = 2\mu_l \frac{\partial^2 u}{\partial z^2} \approx 2\mu_l \frac{u}{h^2}, \tag{5}$$

where $z$ represents the axis perpendicular to the 2-D computational domain, $\mu_l$ is the viscosity of the liquid, $u$ is the maximum vertical speed in a given computational cell, and $h$ is the half thickness of the Hele-Shaw cell. We assume that this relationship is a reasonable approximation even at the finite Reynolds numbers considered in our numerical simulations.

An important attribute of the numerical technique used here is that it entails no tunable parameters to improve the fit between the simulation and the experiment. Instead, the computed flow behavior and the rise speeds emerge self-consistently only from the material parameters and the geometry of the apparatus, much like in an actual laboratory experiment.

### 2.3. Scaling Analysis

The nondimensional numbers emerging from equations (2.2) and (3) are the Reynolds number

$$Re = \frac{\Delta\rho v R_c}{\mu_l}, \tag{6}$$

and the Bond number

$$\mathrm{Bo} = \frac{\Delta\rho g R_c^2}{\sigma}, \tag{7}$$

where we take the radius of the conduit, $R_c$, as the characteristic length, the viscosity of the fluid as the dynamically more relevant viscosity, and the density contrast between the two fluids as the relevant density. The Reynolds number measures the relative importance of inertia to viscous forces in the conduit, and the Bond number quantifies the deformability of the bubbles or slugs. We assume that the Bond number is always above the critical threshold required for slug motion (Bretherton, 1961).

Because the characteristic speed of slugs rising through the conduit is not known a priori in lava lakes, it is not possible to estimate the Reynolds number from material and geometric parameters alone. To relate the Reynolds number only to known parameters, we use a gravitational speed scale $v = \sqrt{gR_c}$. With that definition, the Reynolds number is equivalent to the so-called inverse viscosity number,

$$N_f = \frac{\Delta\rho R_c^{\frac{3}{2}} g^{\frac{1}{2}}}{\mu_l}, \tag{8}$$

commonly used in the analysis of slug dynamics (e.g., James et al., 2006).

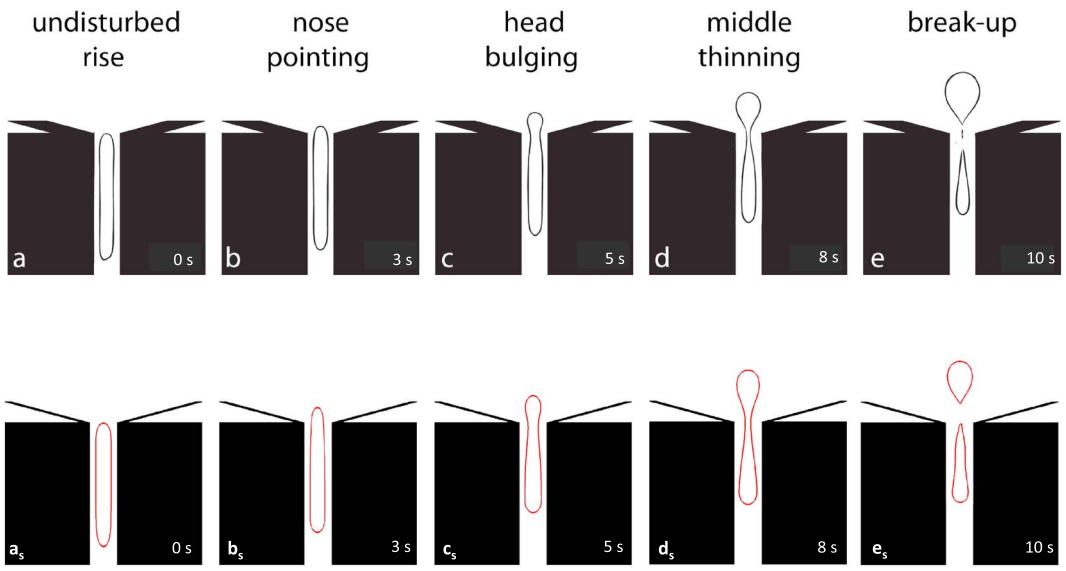


**Figure 5.** Frame sequence from the video recording (upper) and the numerical reproduction (lower) of experiment 75-15-d, illustrating the process of bubble rise and breakup through a high-angle ($\alpha = 75°$) flare geometry: (a and $a_s$) the conduit-filling bubble rises undisturbed in the channel; (b and $b_s$) as it approaches the slope break the head becomes pointed, (c and $c_s$) a few seconds into the flared area the head expands and the middle forms a neck (d and $d_s$) that keeps thinning out until (e and $e_s$) it separates the original bubble into two smaller bubbles.

To define a nondimensional number capturing geometry, we use the cosine of the flare angle (e.g., $\alpha$ in Figure 4) and the aspect ratio, AR, of the slug. We define the aspect ratio as the ratio of the length to the radius,

$$\mathrm{AR} = \frac{L}{R_g}. \tag{9}$$

As discussed in more detail later, these two geometrical parameters can be integrated into a single number for a subset of the experiments.

We also introduce nondimensional numbers that capture the difference in the material properties of the gas and liquid, for example, the viscosity ratio, $M$, defined as

$$M = \frac{\mu_l}{\mu_g}. \tag{10}$$

As we study only the dynamics of gas slugs in viscous fluids, $M$ is extremely large for all cases considered.

## 3. Results

By volcanic standards, lava lakes are characterized by relatively low-viscosity melts, but lava lakes still span a wide nondimensional regime. For example, the phonolite melts from Erebus volcano, Antarctica, probably have viscosities in the range of $10^4$ to $10^6$ Pa s (Giordano et al., 2008) and thus, fall well into the viscosity-dominated regime.

Our laboratory experiments focus on the viscosity-dominated regime to isolate the purely viscous breakup sequence of the slugs passing through the changing geometry in the absence of confounding, inertial effects. We replicate the experiment conditions and then extend the analysis to the inertial regime through numerical simulations.

### 3.1. Breakup in a Diverging Geometry in the Viscous Regime

We performed a total of 48 analog and virtual experiments at low Reynolds numbers or inverse viscosity numbers ($N_f \leq 1$) that varied in the flare angle, $\alpha$, the volume of the gas slug, $V$, and the viscosity of the liquid. The material parameters used in both the laboratory experiments and the simulations are listed in Table 1. We also provide estimates for the key nondimensional numbers and references to the figures that show the behavior observed in a given case. All experiments were based on a Bond number of approximately 40 and very large viscosity ratios.

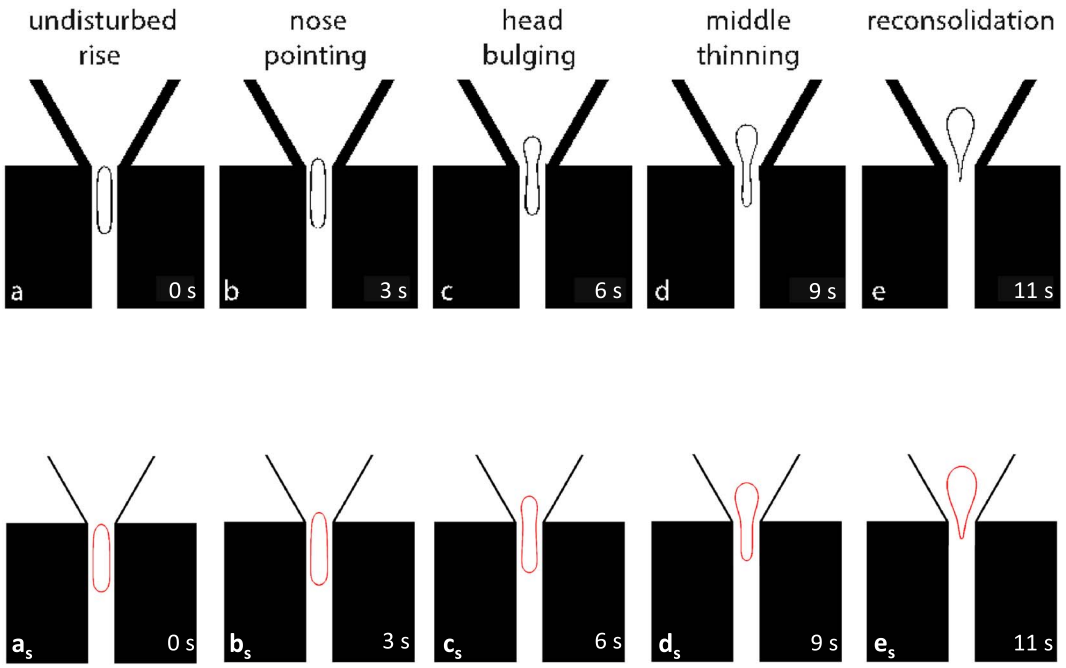


**Figure 6.** Frame sequence from the video recording (upper) and the numerical reproduction (lower) of experiment 30-10-d, illustrating the process of bubble rise and deformation through a small-angle ($\alpha = 30°$) geometry: (a and $a_s$) the conduit-filling bubble rises undisturbed in the channel; (b and $b_s$) as it approaches the slope break the head becomes pointed, (c and $c_s$) a few seconds into the sloped region the head expands and the middle forms a neck (d and $d_s$) that thins out (e and $e_s$) but fails to breakup the bubble, which instead reconsolidates.

A typical breakup sequence of a sufficiently long slug in this regime is shown in Figure 5. Initially, the conduit-filling slug rises undisturbed in the channel (Figures 5a and 5$a_s$). Shortly prior to reaching the break in the slope, the head of the slug becomes pointed (Figures 5b and 5$b_s$). Upon exiting the channel, the slug head bulges outward (Figures 5c and 5$c_s$). As the slug rises through the flaring region, the head continues to expand, and the middle of the slug forms a neck (Figures 5d and 5$d_s$). The neck thins until it separates the original slug into two smaller bubbles (Figures 5e and 5$e_s$).

Overall, the numerical simulations agree well with the experimental data. We observe breakup only for slugs with sufficiently large aspect ratios. Figure 6 shows an example experiment where the slug remains intact as it rises through a relatively narrow flare. Initially, the deformation sequence is similar to the breakup case in Figure 5, including a period of undisturbed rise, head pointing, head bulging, and middle thinning (Figures 6a(6$a_s$)–d(6$d_s$)). However, the thinning process does not split the slug but instead reverses as the slug tail feels the effect of the flare (Figures 6e(6$e_s$)). A comparison of these two sequences suggests that both the aspect ratio of the slug in the straight channel and the flare angle ($\alpha$) play an important role in controlling breakup.

The deformation sequences shown in Figures 5 and 6 suggest that viscous breakup in flaring geometries is determined by the motion of the bubble head relative to its tail. In Figure 7, we plot the position and vertical speed of the slug's highest point (representing the slug head) and lowest point (the slug tail) over time for experiment 30-10-d and the corresponding simulation. The slug does not break up upon passage into the flaring portion of the geometry. The curve representing the motion of the slug head is smooth and steepens gradually when the head enters the flaring area. The tail curve is similar but is steeper once most of the slug is in the flared region. While the bubble propagates inside the channel, the position curves are parallel, meaning that the slug length remains constant, and the bubble is not deforming. In this region, the slug head and tail vertical speed curves (Figure 7b) are superposed and horizontal, meaning that they rise at the same constant speeds. Soon after the head reaches the slope break, the distance between the head and tail position curves increases, which indicates that the slug is stretching in the vertical direction as its head and tail move apart while the middle thins. In the flaring area, the head speed varies slowly and steadily, while the tail speed increases suddenly. Shortly before the tail also reaches the slope break, the slug contracts and eventually

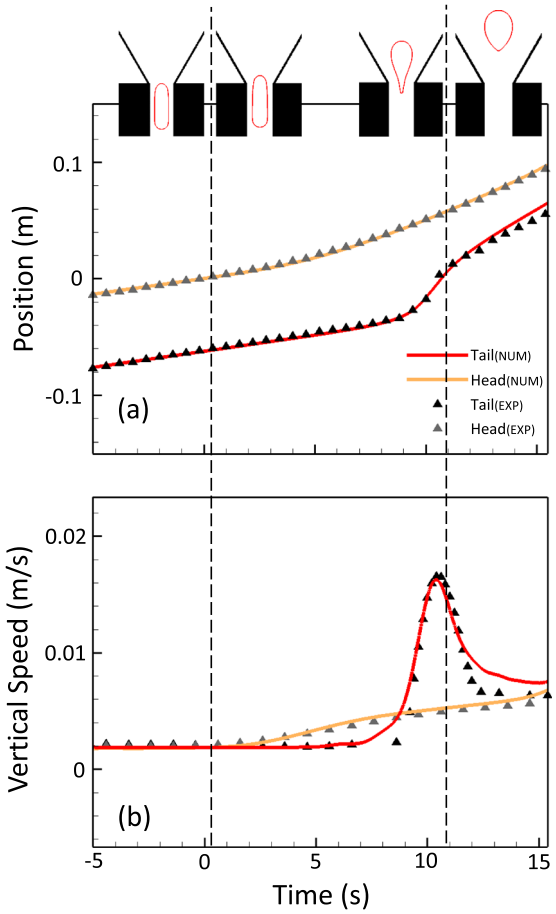


**Figure 7.** Plots of (a) position and (b) vertical speed of the head (highest point) and tail (lowest point) of the gas bubble in experiment 30-10-d and its numerical reproduction, where the bubble does not break up. The triangles and curves represent experimental and numerical results, respectively. The four diagrams at the top are simulations at 0, 3, 10, and 13 s. The two dashed lines represent the moment when the head approaches the slope break and moment when the tail leaves the slope break.

assumes a more rounded shape, as shown by the two position curves approaching each other. When the large bubble reaches the top of the flared region, the entire slug rises at a constant speed, which is greater than that in the narrow channel.

The position and vertical speed curves for the head and tail of a slug that experiences breakup (see Figure 8) are initially similar to those of stable slugs. After the slug breaks up, two new curves appear that represent the motion of the head and tail of the broken-off bubble. The two new curves have the same trend and relative position with respect to their partner curve as expected for a nonbreaking, originally smaller, slug.

### 3.2. Breakup in a Diverging Geometry in the Inertial Regime

The laboratory experiments were performed for only two viscosities, 17 and 49 Pa s, but both cases fall into the viscosity-dominated regime as shown in the supporting information (Figure S2). To assess the dependence of slug stability over a wider nondimensional range, we used direct numerical simulations to upscale the experiments. For this analysis, we keep the Bond number fixed at 40, the same value used in the laboratory experiments.

We find that the stability range of the ascending slugs increases when viscous and inertial effects are similarly important. Figure 9 shows a direct comparison of a simulation in the viscous regime, $N_f \approx 1$, with one where the viscous and inertial effects are important $N_f \approx 23$. As a slug characterized by $N_f \approx 23$ enters the flare, the slug widens in addition to stretching out in the vertical direction. The lateral deformation decreases the degree of the stretching, which is equivalent to reducing the relative difference in the speed of the head and the tail of the slug. The lateral widening also prevents the formation of a thin neck, which precedes an eventual breakup as described in the previous section (see Figure 5). The degree of widening depends sensitively on the angle of the flaring region, as highlighted by comparing the slug deformation in Figures 9a and 9b.

When inertial effects dominate the flow dynamics (e.g., $N_f \approx 116$), however, the stability range decreases (see Figure 10). As the importance of the inertial effects increases, the stagnation pressure in the wake of the slug also increases. As a consequence, the tail of the slug no longer moves at a single well-defined speed, leading to pronounced deformation of the tail and the tearing off of small bubbles on the sides (see Figure 10). Thus, the inertial effects change the mechanism through which breakup occurs. This finding is consistent with previous findings of slug deformation and breakup (e.g., Suckale, Hager, et al., 2010) and is observable in the additional experiments performed in James et al. (2011), where small bubbles are torn off the ascending slug. As a consequence of this breakup, the stable aspect ratio of the gas slugs is reduced significantly in the inertia-dominated regime to slugs that are comparable in width and length, as seen in previous experiments (James et al., 2011) and simulations (Suckale et al., 2011).

The main ramification of this finding is that breakup in the regime of $N_f \approx 116$ depends less on the flare geometry and may occur even in straight conduits (i.e., $\alpha \approx 0°$). At even higher inverse viscosity ($N_f > 116$), the effect of the stagnation pressure becomes increasingly important, and the breakup becomes more pronounced (see supporting information for additional results). As the slugs tend to break up to various degrees within the straight conduit before the slugs reach the flare itself, we do not consider this case further.

We summarize the effect of the inverse viscosity number on bubble stability in Figure 11. The Bond number is 40 for all simulations. Within the range of $0 < N_f < 300$, there is a critical aspect ratio above which bubble breakup occurs, and this critical value decreases with the flare angle, $\alpha$. The curves separating the stability from the breakup regime for different inverse viscosities show that the sensitivity of the breakup to the flare angle varies. At $N_f > 116$, the geometry plays little to no role, and breakup is dominated by the aspect ratio. At

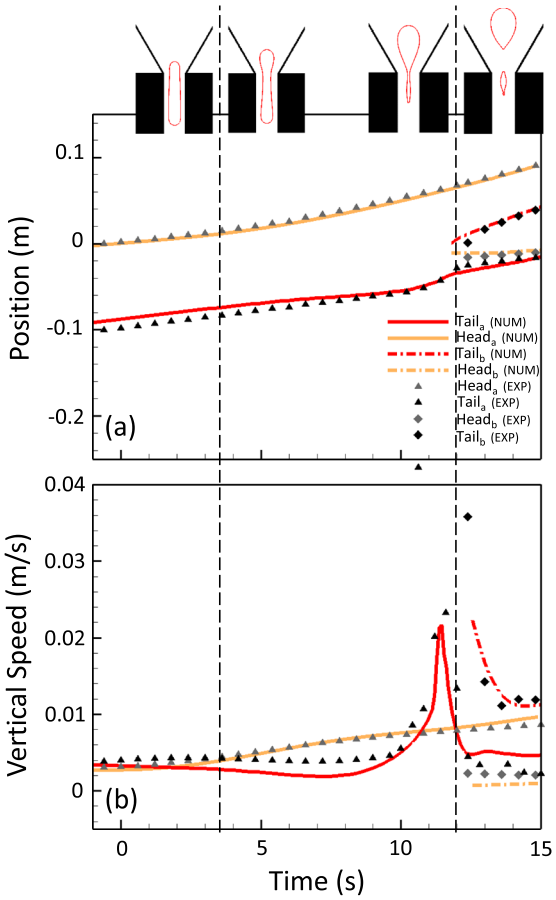


**Figure 8.** Plots of (a) position and (b) vertical speed of the head and tail of the gas bubbles in experiment 30-15-d and its numerical reproduction, where the original gas slug breaks up into two bubbles. Symbols and curves are as in Figure 6 but due to breakup there are additional symbols associated with the additional bubble. The four diagrams at the top are simulations at 3, 7, 11.5, and 14 s. The two dashed lines represent the moment when the stretching begins and the moment when the slug breaks up.

$N_f \approx 23$, the realm of stability is the largest with a critical aspect ratio that is approximately linearly dependent on the cosine of the flare angle. In this regime, the two nondimensional numbers that capture the geometry, the flare angle, and the gas slug aspect ratio, can be integrated into a single number that captures their joint effect, $\cos(\alpha)/\mathrm{AR}$. At $N_f \approx 1$, the flare angle matters only once it exceeds a certain threshold (i.e., $\cos(\alpha) > 0.65$) at which point the flaring increases the speed of the head and thus reduces the stability.

The Bond number has been kept constant so far, partly because the Bond numbers of volcanic slugs tend to be very large and partly because gas slugs only move through narrow channels or pipes if the slugs exceed a critical Bond number (e.g., Bretherton, 1961). There is, however, a slight dependence of breakup on Bond number, as illustrated in Figure 12 for a wide range of Bond numbers ($10^{-1}$ to $10^{13}$) and $N_f \approx 1$. We compare the regime diagrams for two aspect ratios, $\mathrm{AR} = 13$ and $\mathrm{AR} = 7$. At a given aspect ratio, an increase in Bond number increases the tendency of slugs to break up but notably so only if the slug is already close to the critical aspect ratio. The role of the Bond number on the stability of a slug passing through a flare, however, is much less important than that of the flare angle.

### 3.3. Breakup in a Converging Geometry

In a diverging geometry, the breakup of a slug during passage through a flare is related to the stretching that the slug experiences when the head speeds up relative to the tail upon entering the flare (see Figures 7 and 8). This mechanism suggests that in the opposite case, a bubble passing from flaring into more confined geometry, the stability of the bubble should increase because the bubble head would slow down upon entering the confined zone, which would shorten rather than stretch the bubble. We test this hypothesis by turning the apparatus upside down. To initiate the experiment, the bubble is injected into the center of the flaring section and rises toward the narrow channel of the Hele-Shaw cell. All experiments performed upside down are highlighted by the letter UD in Table 1.

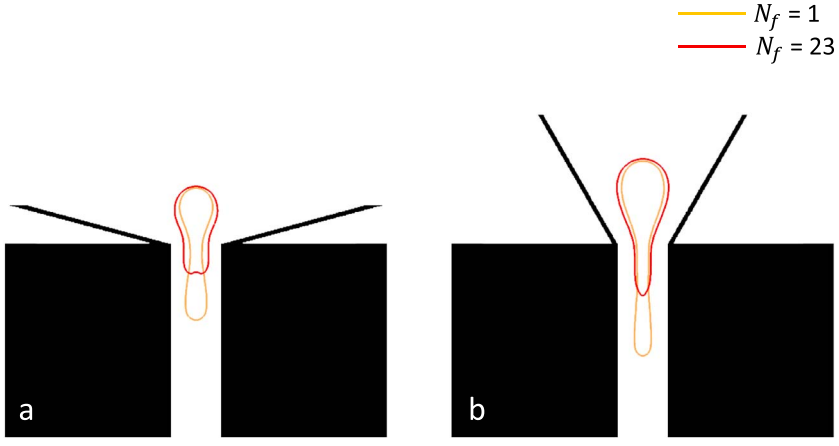


**Figure 9.** Illustration of the head widening mechanism. In plot (a), we compare the reproduction of experiment 75-10-d (yellow) to the simulation with the same AR, $\alpha$, and Bond number, but $N_f \approx 23$ due to lower liquid viscosity (red). In plot (b), we compare the reproduction of experiment 30-15-d (yellow) to the simulation with the same AR, $\alpha$, and Bond number, but $N_f \approx 23$ (red).

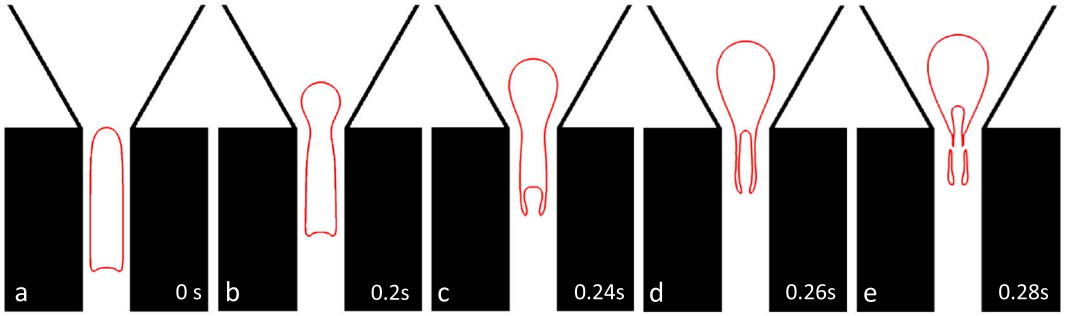


**Figure 10.** Break sequence of the numerical simulation with the same AR, $\alpha$, and Bond number as 30-15-d but higher inverse viscosity ($N_f \approx 116$), illustrating the process of gas slug break up by widening mechanism through a flaring geometry: (a) the conduit-filling bubble rises undisturbed in the channel, a dimple forms at the rear; (b) as it approaches the slope break the head becomes round shape; (c) the head expands and the middle forms a neck, the dimple grows over time; (d) interface thins out at the slug's trailing surface; (e) no stretching breakup occurs, but the thin layer of gas is torn up into several small droplets.

Figure 13 shows the deformation sequence observed in a representative upside-down experiment, UD-30-10-d. Initially, an approximately circular gas bubble approaches a confined channel from the flaring portion of the geometry (Figures 13a and 13a$_s$). Upon reaching the constriction, the bubble deforms significantly to enter the channel, which is smaller than the original radius of the bubble (Figures 13b, 13c and 13b$_s$, 13c$_s$). It then rises stably through the channel (Figures 13d, 13e and 13d$_s$, 13e$_s$). This behavior confirms the expectation that bubbles entering a constriction might be less prone to breakup, at least for small bubbles and/or gradual constrictions.

An alternative behavior is highlighted by example experiment UD-75-10-d, where a bubble approaches a sudden constriction (Figures 14). In this case, the initially circular bubble (Figures 14a and 14a$_s$) deforms as it approaches the channel entrance (Figures 14b and 14b$_s$). The bubble then develops perturbations on the interface that are reminiscent of Rayleigh-Taylor instabilities (Figures 14c and 14c$_s$) but could also be controlled by the downward flow of the liquid from the base of the straight channel as the protruding bubble forces an exchange flow. These instabilities cause the bubble to break into several smaller bubbles (Figures 14d and 14d$_s$) before they enter the straight conduit. When bubbles have different sizes, and thus different rise speeds, daughter bubbles may coalesce again during rise in the channel (Figures 14e and 14e$_s$).

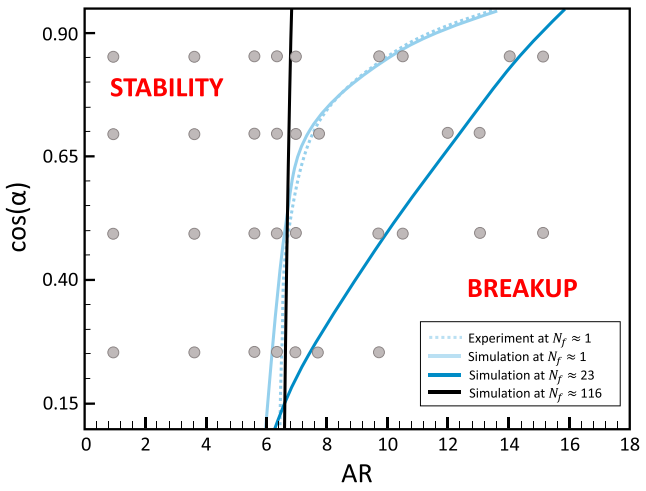


**Figure 11.** Regime diagram for the simulations and experiments at Bo $\approx$ 40. Two of the major factors controlling slug breakup—aspect ratio and flare angle—are plotted against each other. The gray circles mark the conditions of the simulations and experiments done. The solid curves mark the boundary between stability and breakup for simulations at three dimensionless inverse viscosities. The light dashed curve marks the stability transition based on experiments at $N_f \approx 1$.

In the converging configuration, bubble breakup depends primarily on the flare angle and on the aspect ratio of the equivalent conduit-filled slug that has the same volume as the bubble. We plot the regime diagram for the upside-down case in Figure 15. As in the regime diagram for the diverging geometry (i.e., Figure 11), we consider experiments with fixed liquid properties such that $N_f \approx 1$ and Bo $\approx$ 40 for all cases. The smallest bubbles tested (AR = 0.7) are stable for all angles. The larger the angle, the smaller the volume necessary for breakup. When the flare angle decreases to $\alpha \approx 30°$, the bubble does not break up, regardless of its aspect ratio. The numerical reproductions of the experiments are consistent with the regimes.

We upscale the upside-down cases by decreasing the liquid viscosity and observe that inertial effects do not appear to change the critical AR and the critical flare angle of the transition between stability and breakup (see Figure S4 in the supporting information). The results are consistent with the study by James et al. (2006). Within a similar range of inverse viscosity numbers, James et al. (2006) did not observe breakup in their narrowing experiment (which is comparable to the diverging geometry) when the angles are approximately equal or greater than 45° (estimated from Figure 1 in James et al., 2006).

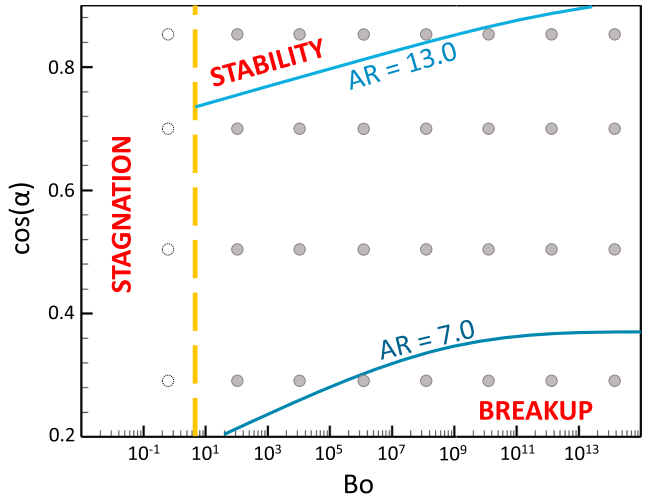


**Figure 12.** Regime diagram for the simulations at $N_f \approx 1$. Two of the major factors controlling bubble breakup—Bond number and the flare angle—are plotted against each other. Two aspect ratios are studied: AR = 13 (light blue curve) and AR = 7 (dark blue curve). An additional field arises at low Bo number (<3, represented by dashed circles): the gas slug is stagnant in the conduit and does not ascend into the flared region.

## 4. Ramifications for Lava Lake Degassing

The experiments and numerical models are 2-D and therefore cannot be used directly to interpret lava lake observations. Nonetheless, this analysis does provide insight into the potential role of lava lake geometry in degassing conditions. As discussed above, constraints on lava lake geometries are limited, particularly regarding the geometry of the connection between the volcanic conduit and the lake (Figure 3). Moreover, this geometry can change with the level of the lake. At Villarica volcano, for example, the lava level within the lava lake could affect the stability of conduit-filling bubbles significantly. The low stand of the lava represents a low-angle flare, while the high stand of the lava is associated with a high-angle flare (Figure 3). At Nyiragongo, the flare angle also changes notably from the low stand (around 30°) to the high stand (around 45°). The situation is different at Erta Ale, where a wide flat bottom exists so that the flare angle remains close to 90° at all lake levels. While no detailed sketches of the geometry of Ray Lake at Erebus volcano are available, we estimate that the flare angle is less than 40° given a lake diameter of 40 m (Calkins et al., 2008) and a lake depth of about 20 m (Oppenheimer et al., 2009). Based on the report by Dibble et al. (2008), who observed a large explosion that exposed the lower portion of Ray Lake, we assume an approximately constant flare angle between 75° and 50° for Erebus. At Hawaii, the recent eruption exposed the geometry of the lava lake flare over more than 200 m. Based on publicly available images (see Figure 1), we estimate the flare angle to be between 20° and 10°.

The stability of bubbles and slugs also depends on the importance of inertial effects, which are controlled by the conduit diameter (Figure 3) and the lava viscosity. Estimates of the diameter of the conduit at the base of Ray Lake vary from 5 to 20 m. Dibble et al. (2008) and Oppenheimer et al. (2009) observed the uppermost conduit of Erebus as 5- to 10-m diameter, after a Strombolian explosion evacuated the lake. Burgi et al. (2014) estimated the conduit diameter of Nyiragongo to be 15 m based on a remarkable draining of the lava

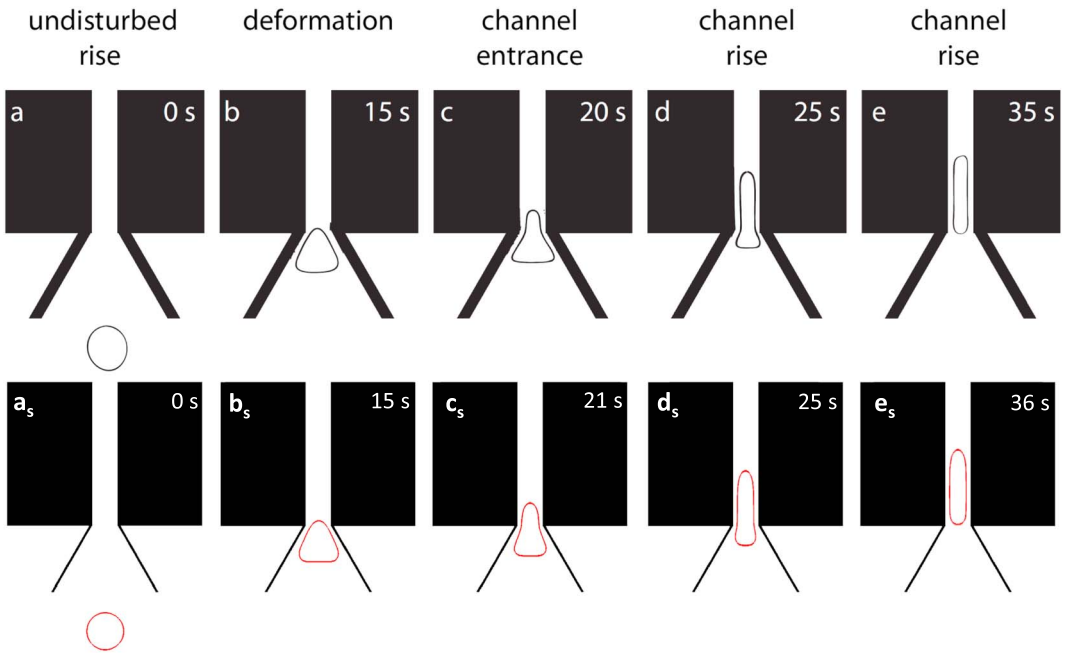


**Figure 13.** Frame sequence from the video recording (upper) and the numerical reproduction (lower) of experiment UD-30-10-d, illustrating the process of bubble rise and deformation through an inverted shallow flaring geometry: (a) the bubble rises undisturbed; (b) as it approaches the slope break it assumes a triangular geometry, (c) the head begins entering the channel (d) slowly followed by the rest of the bubble, (e) which finally forms a slug in the channel.

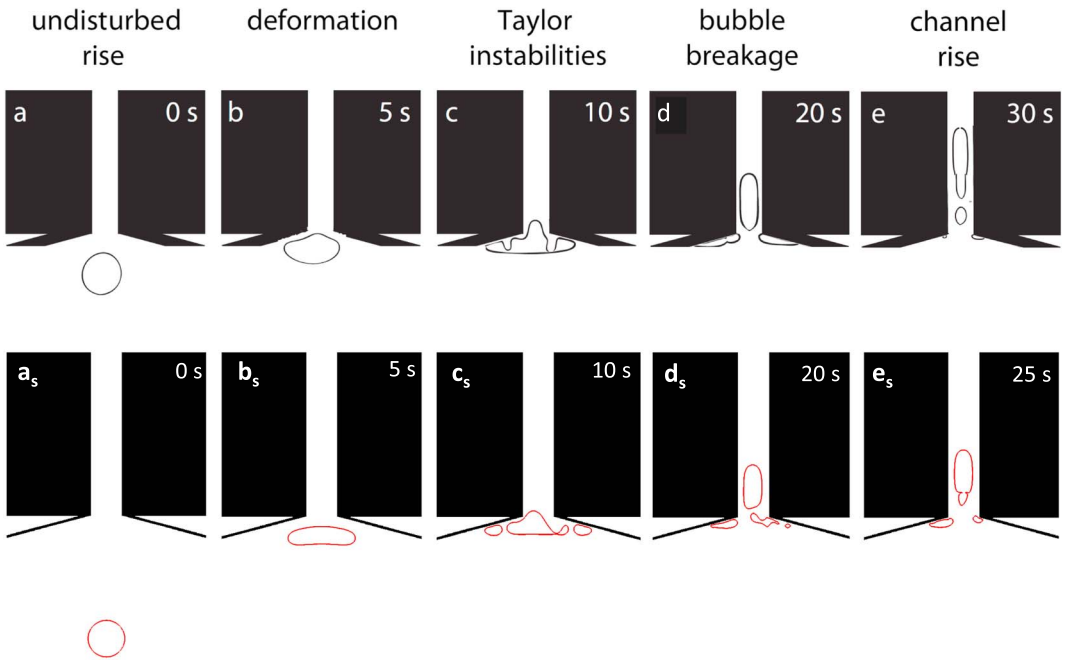


**Figure 14.** Frame sequence from the video recording (upper) and the numerical reproduction (lower) of experiment UD-75-10-d, illustrating the process of bubble rise and deformation through an inverted steep flaring geometry: (a) the bubble rises undisturbed; (b) as it approaches the slope break it deforms; (c) Instabilities begin to develop (d) and grow to separate the bubble into several smaller bubbles, which rise individually in the channel, (e) in some cases coalescing into a single slug.

lake. Palma et al. (2008) and Moussallam et al. (2013) inferred the conduit diameter of Villarica as 10–20 m. We assume that this range of conduit diameters is also appropriate for the lava lakes at Hawaii and Erta Ale, Ethiopia.

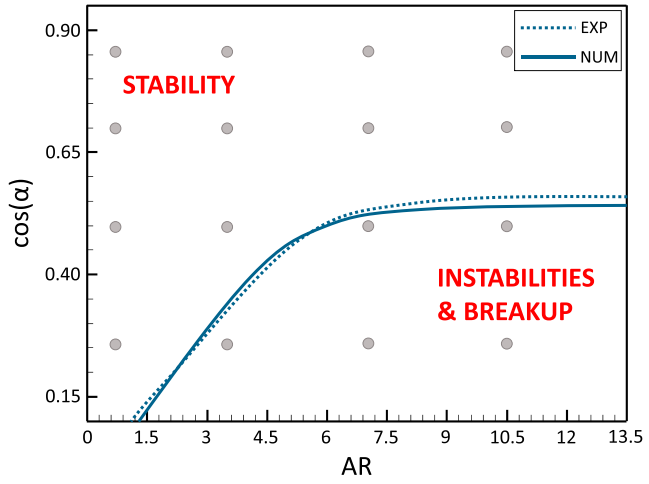


**Figure 15.** Regime diagram for upside-down experiments (rise of bubble through a constriction into a straight channel) and numerical simulations of the same conditions. In all cases, $N_f \approx 1$ and Bo $\approx 40$; the bubble volume (affecting AR) and the flare angle were varied, as indicated by the gray circles. The curve separates conditions where the bubble broke up and conditions where the bubble was stable. Here the simulation and its analog experiment give the same results for stability/instability at all conditions investigated (gray circles). The smallest bubbles (AR = 0.7) were always stable regardless of the flare angle; for bigger bubbles the discriminating factor is the flare angle: bubbles rising through low-angle flares remain cohesive, while bubbles rising through high-angle flares develop gravitational instabilities that lead to breakup.

Lava viscosity can be constrained from published data on melt composition and temperature (Giordano et al., 2008) combined with the volume fraction of bubbles and crystals (e.g., Mader et al., 2013). Most persistentlyactive lava lakes are basaltic. Basaltic melts typically have viscosities of $10^2$–$10^3$ Pa s, depending on the temperature (e.g., Cashman & Mangan, 2014). We assume that this range of viscosities is appropriate for lava lakes such as Halemaumau, Hawaii, and Ambryn, Vanuatu. Lower viscosities are likely associated with hotter temperatures and/or more alkalic basaltic melts, as in the case of Erta Ale, Ethiopia, where we estimate a viscosity of 10–100 Pa s (Vergniolle & Bouche, 2016). The viscosity of Nyiragongo foidite is probably similarly low (i.e., ~60 Pa s; Burgi et al., 2014). Higher viscosities characterize the more crystalline lavas of Villarica, ~500–1,000 Pa s, (Gurioli et al., 2008) and the crystal-bearing phonolite magma of Erebus, which could be as viscous as $10^4$–$10^6$ Pa s (Le Losq et al., 2015). Based on the conduit diameter and the lava viscosity, we estimate the inverse viscosity of the lava lakes as $N_f > 7{,}000$ at Nyiragongo and Erta Ale; $N_f \approx 200$–$7{,}000$ at Hawaii and Ambrym; $N_f \approx 200$–$2{,}000$ at Villarica; and $N_f \approx 0.8$–$30$ at Erebus.

Figure 16 is a regime diagram that considers the effects of the inverse viscosity number, flare angle, and slug aspect ratio, which we compiled to assess the stability of the slugs in the lava lakes. The blue contours indicate the largest stable aspect ratio of the gas slugs observed in our experiments and simulations. The nondimensional regimes spanned by different lava lakes, based on estimates of the flare angle and the inverse viscosity listed above, are marked by dashed lines with various shades of red to

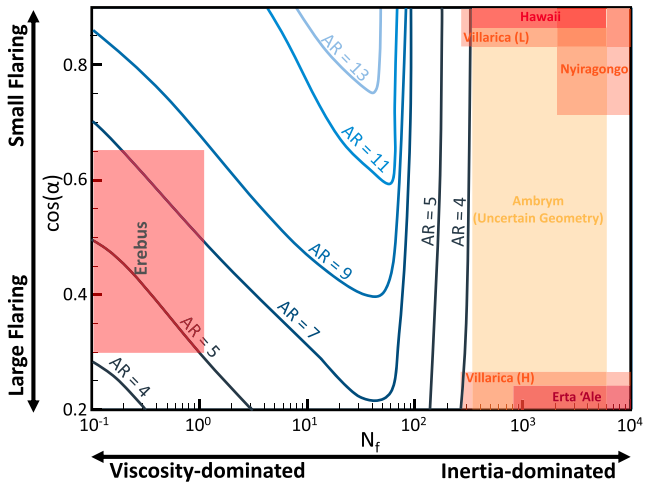


**Figure 16.** Regime diagram for the simulations with varying aspect ratios at Bo $\approx 10^7$ based on the two major factors controlling bubble breakup—inverse viscosity and flare angle. The transition between breakup and stability for varying aspect ratios is shown by the blue contours. The contour label indicates the maximum AR that is stable along that curve; the label is on the side of the contour where slugs of that AR value are stable. Based on the estimated inverse viscosity and flare angle, lava lakes fall into different regions marked by semitransparent colored boxes. (H) and (L) represent the high stand and low stand shown in Figure 3.

distinguish the different lava lakes. Most lava lakes fall well within the range of slug breakup, mostly because of their relatively high inverse viscosity. Erebus spans the widest range of aspect ratios for which gas slugs are stable, because its lava has a notably higher viscosity than the other lava lakes. In this case, the largest stable aspect ratio is controlled mostly by the flare angle. For most other lakes, slug stability is governed primarily by the flow dynamics captured by the inverse viscosity number. For example, despite the dramatic variations in the flare angle for the low (L) and high (H) stands of the lava lake at Villarica, the geometry likely exhibits little control over the degassing patterns. The critical aspect ratio for slug breakup is likely around 4 for the high and low stands. We anticipate a similar aspect ratio for Hawaii, Nyiragongo, Ambrym, and Erta Ale, although the flare angle of the lava lake at Ambrym is not well constrained. All of these lava lakes fall into a regime where the flare angle is probably not very consequential for slug stability.

Compared to other lava lakes, our results suggest that slugs are most prone to break up at Erta Ale and Nyiragongo, because of a higher inverse viscosity than in the case of Hawaii and Ambrym. We find that in these cases, slugs break up before they reach the flare region. This prediction is consistent with visual observations of chaotic bubbling on the lava lake surface at Ambrym (Allard et al., 2016) and supported by measurements of persis-

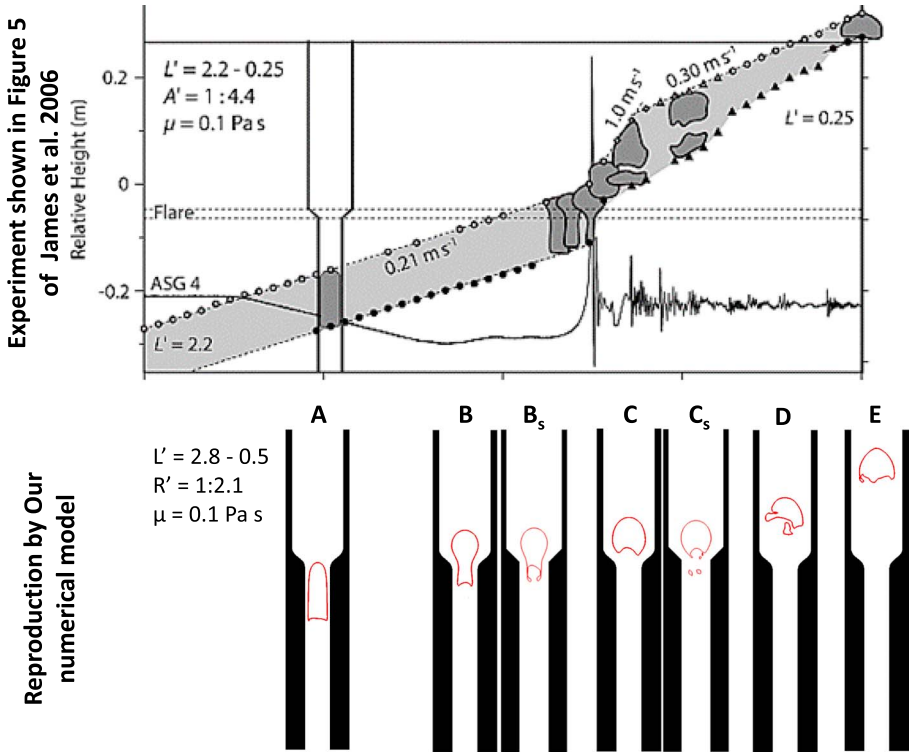


**Figure 17.** Reproduction of a laboratory experiment reported by James et al. (2006). The upper picture is Figure 5b of James et al. (2006); the lower diagram shows the 2-D simulation with the same viscosity ($\mu_l = 0.1$ Pa s) and the same geometry as the laboratory experiment (ratio of the narrow tube radius to the wide tube radius, $R' = (A')^{1/2} = 1 : 2.1$; $\alpha \approx 45°$; smoothed corners) . $L'$ represents the ratio of the vertical length of gas slug to the tube diameter. Here $N_f \approx 290$ and Bo $\approx 50$. While obviously different in the exact interface shapes, both show that the slug does not break up when passing through the flare (A–C), but rather breaks up later due to nonlinearities in the pressure wake (D) and eventually reconstitutes (E). To investigate the effect of the sharpness of the flare on the stability, we also reran the simulation with a sharp connection for the two tubes and show the results in $B_s$ and $C_s$.

tent gas emissions at Erta Ale and Nyriagonga that suggest the presence of multiple smaller bubbles, rather than a single, conduit-filling slug (e.g., Sawyer et al., 2008).

We note that a detailed investigation of slug stability at inverse viscosity above 1,000 is not the main purpose of this study and that more work is needed to reliably predict stable slug sizes in this regime. The 2-D geometry of the experimental and numerical setups is not well suited for resolving nonlinear, inertial effects, and a 3-D approach as in Ambrose et al. (2017) would be more suitable. That being said, slug breakup rising through straight conduits in the inertial regime has also been observed in previous experiments (e.g., James et al., 2006, 2011; Pringle et al., 2015) and in simulations (e.g., Ambrose et al., 2017; Suckale, Hager, et al., 2010; Suckale et al., 2011). The results of these studies are consistent with the present study results in the sense that those results showed more pronounced breakup in the inertial regime (James et al., 2006) and in noticing that geometry is not necessarily the main controlling factor in this regime.

In Figure 17, we perform a more direct comparison of the simulations with the experimental results by James et al. (2006). As shown in the upper frame of Figure 17 reproduced from James et al. (2006), a gas slug ascends from a small- to a large-diameter tube. In this experiment, the two tubes are connected by a short smooth reducer, and the inverse viscosity number is approximately 290. Our numerical model with the same geometry reproduces the experiment slug dynamics (see Figure 17A, B, C, and D). The slug ascends into the larger tube without breaking up at the flare but breaks up shortly after entering the large tube. In Figure 17Bs and Cs, we show an equivalent simulation of a slug with $N_f = 290$ rising through a geometry that is characterized by a sharp transition between the conduit and the flare. Although the difference in the geometry between Figure 17B and Bs and Figure 17C and Cs is subtle, the consequence on slug stability is notable. The presence of a sharp transition between the conduit and the flare leads to tearing off of small bubbles as the slug enters the flare. This comparison leads us to conclude that the difference in the breakup morphology is related to a slight difference in the geometry, again accentuating the importance of geometrical affects on slug ascent and stability.

## 5. Conclusion

Analog laboratory experiments have made invaluable contributions to our understanding of volcanic systems, but such experiments do not always translate in a straightforward way to the inevitably much more complex natural system. Here we complement analog experiments with numerical simulations to facilitate the generalization of laboratory insights to volcanic systems. Instead of attempting to capture the full complexity of lava lakes, we focus on understanding how a single parameter, the flare angle of the lava lake, may affect the stability of gas slugs in viscosity- and inertia-dominated regimes.

A key finding of the present analysis is that slug breakup is controlled by different mechanisms depending on the geometry and the relative importance of the viscous and inertial effects. As a gas slug exits the conduit into the lava lake flare in the viscosity-dominated regime, breakup occurs through stretching and splitting of the slug. At $N_f \approx 23$, slugs are the most stable, because they deform in the vertical and lateral directions, which reduces vertical stretching and, thus, the tendency to break up. At $N_f > 116$, an additional breakup mechanism becomes pertinent as stagnation pressure creates an increasingly pronounced indent in the wake of the slug that leads to the creation of small bubbles along the sides.

Applying this result to currently active lava lakes, we find that most lava lakes fall into a nondimensional regime where slug breakup is expected to limit the maximum aspect ratio of the slugs to approximately 4, even in the absence of additional perturbations that may be associated with thermal convection, faltering lava lake crust, or other heterogeneities. This conclusion depends heavily on the viscosity estimates for these lava lakes and could be reassessed based on the regime diagram in Figure 16 when additional data become available.

**Acknowledgments**
We acknowledge summer support for Liannie Velazquez Santana through the Stanford SURGE program. A. S. wishes to acknowledge M. Rosi for enabling this scientific collaboration, as well as the Erasmus program and the University of Pisa Thesis Abroad program for financial support. Laboratory work was supported by NERC grant NE/G016593/1. The code and data used in this study are available through GitLab at http://zapad.stanford.edu/sigma/Gas-slug-Geometry. Z. Q. performed the numerical simulations and compared the numerical and experimental results. A. S. performed the laboratory experiments. L. C. V. S. performed the initial numerical simulations for validation and upscaling. A. C. R. conceptualized the laboratory experiments and supported their analysis. J. S. contributed to the analysis of the numerical simulation. K. V. C. compiled the lava lake geometries. All authors contributed to the text.

## References

Allard, P., Burton, M., Sawyer, G., & Bani, P. (2016). Degassing dynamics of basaltic lava lake at a top-ranking volatile emitter: Ambrym volcano, Vanuatu arc. *Earth and Planetary Science Letters*, *448*, 69–80.

Ambrose, S., Lowndes, I. S., Hargreaves, D. M., & Azzopardi, B. (2017). Numerical modelling of the rise of Taylor bubbles through a change in pipe diameter. *Computers and Fluids*, *148*, 10–25.

Aster, R., Mah, S., Kyle, P., McIntosh, W., Dunbar, N., Johnson, J., et al. (2003). Very long period oscillations of Mount Erebus volcano. *Journal of Geophysical Research*, *108*(B11), 2522. https://doi.org/10.1029/2002JB002101

Bagdassarov, N., & Pinkerton, H. (2004). Transient phenomena in vesicular lava flows based on laboratory experiments with analogue materials. *Journal of Volcanology and Geothermal Research*, *132*(2-3), 115–136.

Beckett, F., Mader, H., Phillips, J., Rust, A., & Witham, F. (2011). An experimental study of low-Reynolds-number exchange flow of two Newtonian fluids in a vertical pipe. *Journal of Fluid Mechanics*, *682*, 652–670.
Blackburn, E. A., Wilson, L., & Sparks, R. S. J. (1976). Mechanisms and dynamics of Strombolian activity. *Journal of the Geological Society of London*, *132*(4), 429–440.
Borhan, A., & Pallinti, J. (1999). Breakup of drops and bubbles translating through cylindrical capillaries. *Physical Fluids*, *11*(10), 2846–2855.
Bouche, E., Vergniolle, S., Staudacher, T., Nercessian, A., Delmont, J.-C., Frogneux, M., et al. (2010). The role of large bubbles detected from acoustic measurements on the dynamics of Erta 'Ale lava lake (Ethiopia). *Earth and Planetary Science Letters*, *295*(1), 37–48.
Bretherton, F. P. (1961). The motion of long bubbles in tubes. *Journal of Fluid Mechanics*, *10*(2), 166–188.
Burgi, P.-Y., Darrah, T., Tedesco, D., & Eymold, W. (2014). Dynamics of the Mount Nyiragongo lava lake. *Journal of Geophysical Research: Solid Earth*, *119*, 4106–4122. https://doi.org/10.1002/2013JB010895
Calder, E. S., Harris, A. J., Pe na, P., Pilger, E., Flynn, L. P., Fuentealba, G., & Moreno, H. (2004). Combined thermal and seismic analysis of the Villarrica volcano lava lake, chile. *Revista Geol'ogica de Chile*, *31*(2), 259–272.
Calkins, J., Oppenheimer, C., & Kyle, P. R. (2008). Ground-based thermal imaging of lava lakes at Erebus volcano, Antarctica. *Journal of Volcanology and Geothermal Research*, *177*(3), 695–704.
Cashman, K. V., & Mangan, M. (2014). A century of studying effusive eruptions in Hawai'i, *Characteristics of Hawaiian volcanoes* (pp. 357–390). Reston, VA: U.S. Geological Survey.
Daly, R. A. (1911). The nature of volcanic action In Proceedings of the American Academy of Arts and Sciences (pp. 47–122). JSTOR.
Dibble, R. R., Kyle, P. R., & Rowe, C. A. (2008). Video and seismic observations of Strombolian eruptions at Erebus volcano, Antarctica. *Journal of Volcanology and Geothermal Research*, *177*(3), 619–634.
Gerst, A., Hort, M., Aster, R., Johnson, J., & Kyle, P. (2013). The first second of volcanic eruptions from the Erebus volcano lava lake, Antarctica: Energies, pressures, seismology, and infrasound. *Journal of Geophysical Research: Solid Earth*, *118*, 3318–3340. https://doi.org/10.1002/jgrb.50234
Giordano, D., Russell, J. K., & Dingwell, D. B. (2008). Viscosity of magmatic liquids: A model. *Earth and Planetary Science Letters*, *271*(1-4), 123–134.
Gurioli, L., Harris, A. J., Houghton, B. F., Polacci, M., & Ripepe, M. (2008). Textural and geophysical characterization of explosive basaltic activity at Villarrica volcano. *Journal of Geophysical Research*, *113*, 1–16. https://doi.org/10.1029/2007JB005328
James, M., Lane, S. J., & Chouet, B. (2006). Gas slug ascent through changes in conduit diameter: Laboratory insights into a volcano-seismic source process in low-viscosity magmas. *Journal of Geophysical Research*, *111*, B05201. https://doi.org/10.1029/2005JB003718
James, M. R., Llewellin, E. W., & Lane, S. J. (2011). Comment on "It takes three to tango: 2. Bubble dynamics in basaltic volcanoes and ramifications for modeling normal Strombolian activity" by J. Suckale, B.H. Hager, L.T. Elkins-Tanton, and J.-C. Nave. *Journal of Geophysical Research*, *116*, B06208. https://doi.org/10.1029/2011JB008351
Jaupart, C., & Vergniolle, S. (1989). The generation and collapse of a foam layer at the roof of a basaltic magma chamber. *Journal of Fluid Mechanics*, *203*, 347–380.
Johnson, J., Aster, R., Jones, K. R., Kyle, P., & McIntosh, B. (2008). Acoustic source characterization of impulsive strombolian eruptions from the Mount Erebus lava lake. *Journal of Volcanology and Geothermal Research*, *177*(3), 673–686.
Le Losq, C., Neuville, D. R., Moretti, R., Kyle, P. R., & Oppenheimer, C. (2015). Rheology of phonolitic magmas—The case of the Erebus lava lake. *Earth and Planetary Science Letters*, *411*, 53–61.
Llewellin, E. W., Mader, H. M., & Wilson, S. D. R. (2002). The rheology of a bubbly liquid. *Proceedings of the Royal Society of London A*, *458*(2020), 987–1016.
Mader, H. M., Llewellin, E. W., & Mueller, S. P. (2013). The rheology of two-phase magmas: A review and analysis. *Journal of Volcanology and Geothermal Research*, *257*, 135–158.
Moussallam, Y., Bani, P., Curtis, A., Barnie, T., Moussallam, M., Peters, N., et al. (2016). Sustaining persistent lava lakes: Observations from high-resolution gas measurements at Villarrica volcano, Chile. *Earth and Planetary Science Letters*, *454*, 237–247.
Moussallam, Y., Oppenheimer, C., Scaillet, B., & Kyle, P. R. (2013). Experimental phase-equilibrium constraints on the phonolite magmatic system of Erebus volcano, Antarctica. *Journal of Petrology*, *54*(7), 1285–1307.
Oppenheimer, C., Lomakina, A. S., Kyle, P. R., Kingsbury, N. G., & Boichu, M. (2009). Pulsatory magma supply to a phonolite lava lake. *Earth and Planetary Science Letters*, *284*(3-4), 392–398.
Osher, S., & Sethian, J. A. (1988). Fronts propagating with curvature-dependent speed: Algorithms based on Hamilton-Jacobi formulations. *Journal of Computational Physics*, *79*(1), 12–49.
Palma, J. L., Calder, E. S., Basualto, D., Blake, S., & Rothery, D. A. (2008). Correlations between $SO_2$ flux, seismicity, and outgassing activity at the open vent of Villarrica volcano, Chile. *Journal of Geophysical Research*, *113*, 1–23. https://doi.org/10.1029/2008JB005577
Parfitt, E., & Wilson, L. (1995). Explosive volcanic eruptions-IX. The transition between Hawaiian-style lava fountaining and Strombolian explosive activity. *Geophysical Journal International*, *121*(1), 226–232.
Patrick, M., Wilson, D., Fee, D., Orr, T., & Swanson, D. (2011). Shallow degassing events as a trigger for very-long-period seismicity at Kilauea volcano, Hawai'i. *Bulletin of Volcanology*, *73*(9), 1179–1186.
Perret, F. A. (1913). The lava fountains of Kilauea. *American Journal of Science*, *35*(206), 139–148.
Pioli, L., Azzopardi, B., & Cashman, K. (2009). Controls on the explosivity of scoria cone eruptions: Magma segregation at conduit junctions. *Journal of Volcanology and Geothermal Research*, *186*(3), 407–415.
Pringle, C. C., Ambrose, S., Azzopardi, B. J., & Rust, A. C. (2015). The existence and behaviour of large diameter Taylor bubbles. *International Journal of Multiphase Flow*, *72*, 318–323.
Pyle, D., Pinkerton, H., Norton, G., & Dawson, J. (1995). Carbonatite volcanism: Ol Doinyo Lengai and the petrogenesis of natrocarbonatites, *The dynamics of degassing at Ol Doinyo Lengai*. Berlin: Springer, pp. 37–46.
Qin, Z., Delaney, K., Riaz, A., & Balaras, E. (2015). Topology preserving advection of implicit interfaces on Cartesian grids. *Journal of Computational Physics*, *290*, 219–238.
Qin, Z., & Suckale, J. (2017). Direct numerical simulations of gas-solid-liquid interactions in dilute fluids. *International Journal of Multiphase Flow*, *96*, 34–47.
Rust, A. C., & Manga, M. (2002). Bubble shapes and orientations in low Re simple shear flow. *Journal of Colloid and Interface Science*, *249*(2), 476–480.
Sawyer, G. M., Carn, S. A., Tsanev, V. I., Oppenheimer, C., & Burton, M. (2008). Investigation into magma degassing at Nyiragongo volcano, Democratic Republic of the Congo. *Geochemistry, Geophysics, Geosystems*, *9*, Q02017. https://doi.org/10.1029/2007GC001829
Suckale, J., Hager, B. H., Elkins-Tanton, L. T., & Nave, J.-C. (2010). It takes three to tango: 2. Bubble dynamics in basaltic volcanoes and ramifications for modeling normal Strombolian activity. *Journal of Geophysical Researc*, *115*, B07410. https://doi.org/10.1029/2009JB006917

Suckale, J., Hager, B. H., Elkins-Tanton, L. T., & Nave, J.-C. (2011). Reply to the comment by Mike R. James et al. on "It takes three to tango: 2. Bubble dynamics in basaltic volcanoes and ramifications for modeling normal Strombolian activity". *Journal of Geophysical Research*, *116*, B06208. https://doi.org/10.1029/2011JB008351

Suckale, J., Nave, J.-C., & Hager, B. H. (2010). It takes three to tango: 1. Simulating buoyancy-driven flow in the presence of large viscosity contrasts. *Journal of Geophysical Researc*, *115*, B07409. https://doi.org/10.1029/2009JB006916

Swanson, D. A., Duffield, W. A., Jackson, D. B., & Peterson, D. W. (1979). Chronological narrative of the 1969–71 Mauna Ulu eruption of Kilauea volcano, Hawaii. Washington: U.S. Geological Survey Professional Paper.

Vergniolle, S., & Bouche, E. (2016). Gas-driven lava lake fluctuations at Erta 'Ale volcano (Ethiopia) revealed by MODIS measurements. *Bulletin of Volcanology*, *78*(9), 60.

Vergniolle, S., & Jaupart, C. (1990). Dynamics of degassing at Kilauea volcano, Hawaii. *Journal of Geophysical Research*, *95*(B3), 2793.

Vergniolle, S., & Mangan, M. (2000). Hawaiian and Strombolian eruptions. Encyclopedia of Volcanoes, 447-461.

Wilson, L., & Head, J. W. (1981). Ascent and eruption of basaltic magma on the Earth and Moon. *Journal of Geophysical Research*, *86*(B4), 2971–3001.

Witham, F., Woods, A. W., & Gladstone, C. (2006). An analogue experimental model of depth fluctuations in lava lakes. *Bulletin of Volcanology*, *69*(1), 51–56.